

 Open access • Journal Article • DOI:10.1007/S10548-013-0313-Y

Influence of skull modeling approaches on EEG source localization — [Source link](#)

[Victoria Montes-Restrepo](#), [Pieter van Mierlo](#), [Gregor Strobbe](#), [Steven Staelens](#) ...+2 more authors

Institutions: [Ghent University](#), [Katholieke Universiteit Leuven](#)

Published on: 01 Jan 2014 - [Brain Topography](#) (Springer US)

Topics: [Human head](#)

Related papers:

- [Modeling of the human skull in EEG source analysis](#)
- [A guideline for head volume conductor modeling in EEG and MEG.](#)
- [The electrical conductivity of human cerebrospinal fluid at body temperature](#)
- [Influences of skull segmentation inaccuracies on EEG source analysis.](#)
- [EEG source analysis of epileptiform activity using a 1 mm anisotropic hexahedra finite element head model.](#)

Share this paper:    

View more about this paper here: <https://typeset.io/papers/influence-of-skull-modeling-approaches-on-eeeg-source-2f9a4jyxt7>

Influence of skull modeling on EEG source localization: Inhomogeneities, geometry and noise sensitivity

Victoria Montes-Restrepo¹, Hans Hallez^{1,2}, Pieter van Mierlo¹ and Steven Staelens^{1,3}

¹ Faculty of Engineering, Medical Image and Signal Processing (MEDISIP), IBBT, Ghent University, De Pintelaan 185, 9000 Ghent, Belgium

² Faculty of Engineering Technology, Electronics/ICT, Catholic University College of Bruges-Ostend (KHBO), Zeedijk 101, 8400 Oostende, Belgium

³ Faculty of Medicine, Molecular Imaging Center Antwerp (MICA), Antwerp University, Wilrijkstraat 10, 2650 Edegem, Belgium

E-mail: Victoria.MontesRestrepo@UGent.be

Abstract. We investigated the influence of using simplified models for the skull on electroencephalogram (EEG) source localization. A head model with an accurately segmented skull from computed tomography (CT) images, including spongy and compact bones as well as some air-filled cavities, was used as reference. The simplifications were first assumed for the skull conductivity modeling as: (1) isotropic heterogeneous in which the spongy layer was segmented as an erosion of the compact layer, (2) anisotropic homogeneous and (3) isotropic homogeneous. Furthermore, the effect of simplifying the geometry of the skull through the use of MR-based skulls was also investigated generating the following models: (4) isotropic heterogeneous with the spongy bone segmented from MR, (5) isotropic heterogeneous with the spongy bone segmented as an erosion of the compact bone, (6) anisotropic homogeneous and (7) isotropic homogeneous. All the simulations were performed for a configuration of 32 and 128 electrodes and with the addition of gaussian noise with three SNRs: 0, 5 and 10 dB. The results suggest that ...

1. Introduction

Electroencephalogram (EEG) source localization is a commonly used tool in the pre-surgical evaluation of patients affected by epilepsy [3]. This technique aims at reconstructing the electrical sources inside the brain from its potentials measured on the scalp surface. In order to achieve this goal, two subproblems have to be solved: (i) the *forward* problem, which determines the electrode potentials at the scalp given a source description, and (ii) the *inverse* problem, in which the source parameters are estimated given a measured set of electrode potentials.

To model the active sources inside the brain, current dipoles are usually used [25]. In addition to the source description, the generation of a model accurately representing the human head is an important requirement for the solution of the forward problem. Head models range in complexity from spherical [4, 9] with an analytical solution to realistically shaped [7, 20] with a numerical solution. In the realistic models, the geometry and conductivity values of the different tissues inside the head need to be incorporated. Particularly, the conductivity of the *skull* is very low compared to the other tissues, which causes an attenuation on the surface measurements. Consequently, the skull plays an important role in EEG source localization.

The most simplified model for the skull consists of an isotropic homogeneous single compartment, often with an approximate geometry. This model has been frequently applied [35, 33] due to its simplicity and possibility to incorporate in spherical as well as in boundary element models (BEM). However, the actual structure of the skull is three-layered, consisting of a spongiform layer surrounded by two compact layers. Not only spongiform and compact bones are part of this structure but also air-filled cavities such as the paranasal sinuses and mastoid cells. Therefore, the skull has different conductivities and thicknesses throughout its whole structure and so it is *inhomogeneous*.

The concept of *anisotropy* was introduced as a way to model the inhomogeneities due to the layered structure of the skull. For the characterization of anisotropic conductivity, two directions, radial and tangential, have to be defined. Rush and Driscoll reported the first measurements for these directional conductivities of the skull, deducing an anisotropy ratio of 1:10 (radial:tangential) [30]. However, recent studies have suggested that the skull anisotropy must be lower than that, i. e., around 1:1.6 [12, 31, 8].

Anisotropy has been commonly used to model the skull conductivity in many applications [22, 37, 29, 15]. This approach was used because the imaging and computer technologies were not advanced enough to visualize and handle the detailed structure of the skull. With the advances in imaging modalities and the increase in computational power, all the anatomical details that are available from magnetic resonance (MR) and computed tomography (CT) images, such as fluid filled spaces and inhomogeneities in the skull, can be incorporated into the head model [28, 31, 8].

MRI is a well-known technique for the visualization of the anatomical structure of the head. However, the skull bone cannot be easily reconstructed solely from these images. In contrast, CT images get a correct representation of the skull but are not commonly performed on patients due to the ionizing radiation. As a consequence, the accurate segmentation of the geometry of the skull and its layered structure remains unresolved.

In this work we analyze the influence of using simplified models for the skull on EEG source localization. For this purpose, co-registered MR and CT images of one patient are available. A head model with an accurately segmented skull, including spongy and compact bones as well as some air-filled cavities, is incorporated in the analysis as a

reference model. Two types of simplification: (i) conductivity modeling and (ii) geometry are performed on the skull, generating seven different models. In order to assess the effect of spatial sampling, the study is accomplished for two electrode configurations: 32 and 128. Furthermore, we also investigate the effect of noise on the dipole estimation for the different models. The influence of the conductivity values for the different tissues is beyond the scope of this work.

The questions that we sought to answer through this study were: (i) “when the skull geometry is segmented from CT, which conductivity modeling gives the lower dipole estimation errors: isotropic heterogeneous, anisotropic homogeneous or isotropic homogeneous?”; (ii) “when the skull geometry is segmented from MR, which of the previous conductivity modeling options introduces less errors in the localization process?”; (iii) “how sensitive are the models to the addition of noise?” and (iv) “which errors are made when a lower number of electrodes are used?”. Finally, the most important goal is the determination of guidelines for skull modeling in the generation of subject-specific head models in a clinical setup of epilepsy.

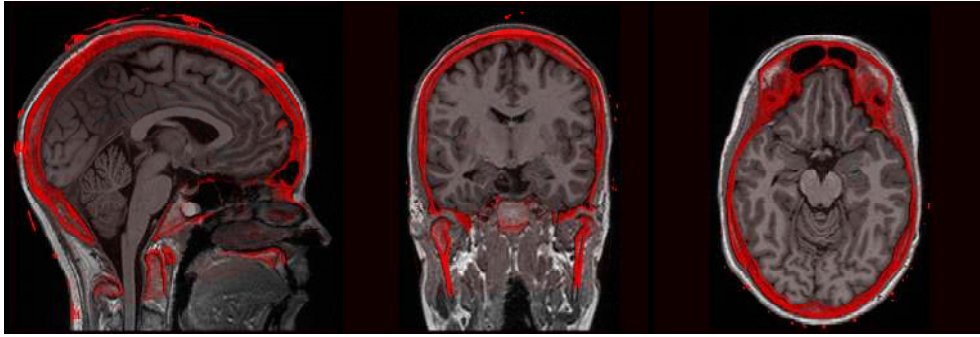
2. Methods

2.1. Head model construction

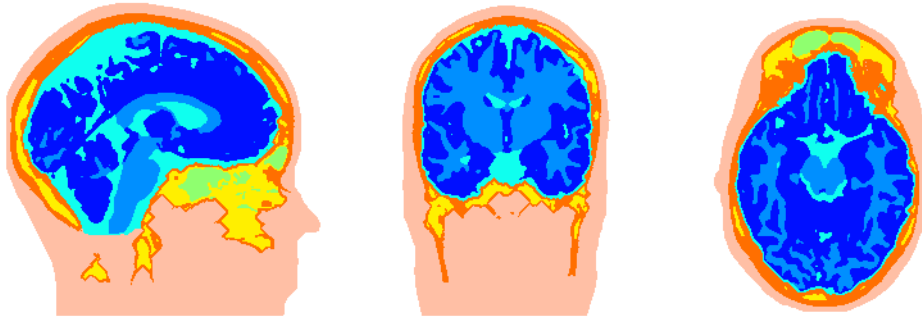
Different realistic head models were generated from MR and CT images of one patient from the database of the reference center of epilepsy of the department of neurology at the Ghent University Hospital (Belgium). The MR images were acquired using a 3T scanner (Siemens Trio, Erlangen, Germany) and consisted of a $256 \times 256 \times 176$ matrix with voxels of $0.86 \text{ mm} \times 0.86 \text{ mm} \times 0.9 \text{ mm}$. These images were used to segment the scalp and brain tissues. The scalp was segmented through thresholding followed by a closing with hole filling operation. The segmentation of cerebrospinal fluid (CSF), white matter (WM) and grey matter (GM) was done with the SPM8 toolbox [11].

The CT images (Toshiba Aquilion, Tokyo, Japan), coregistered with the MR, were used to accurately segment the skull. These images were first preprocessed in order to remove artefacts such as those caused by the presence of electrodes during the acquisition. Posteriorly, a CT/MR thresholding approach followed by morphological operations such as dilation and erosion were performed in order to obtain the skull compartment. To distinguish between compact and spongy bones as well as air cavities, thresholding was applied according to the intensity levels displayed in the histogram. The thickness of the skull was kept within the normal limits for an adult skull [21]. Figure 1a shows the MR image of the patient used in this study with the CT overlaid in red.

In order to perform a comparison between different models for the skull, a *reference* model or *ground truth* was established. This reference head model incorporates a realistic



(a) MR with overlaid CT image in red.



(b) Segmented reference head model.

Figure 1: Reference head model in sagittal, coronal and axial views, showing seven different tissue types: ■ Scalp, ■ CSF, ■ WM and ■ GM segmented from MR; ■ Compact bone, ■ Spongy bone and ■ Air cavities, all segmented from CT.

geometry for the skull, consisting of separate isotropic layers for the compact and spongy bone compartments in addition to air-filled cavities such as the frontal and sphenoidal sinuses (Figure 1b). These cavities were assumed to have the conductivity of air, i.e., null conductivity. The conductivities for the compact and spongy bones were chosen according to the measurements of [1] as: $\sigma_{\text{comp}} = 0.0064$ S/m and $\sigma_{\text{spong}} = 0.02865$ S/m. Table 1 shows the conductivity values for all the tissues in the reference head model. The segmentation of the head model was checked manually. A post-processing step allowed to optimize the segmented model. Particularly, GM and WM layers were surrounded by CSF ensuring that these tissues were not in direct contact with the compact bone. Also, it was guaranteed that compact bone was surrounding both spongy bone and air cavities. In this way, a forward solution can be found.

The influence of the skull on dipole estimation is analyzed through the generation of different models based on the simplification of the skull. In the following subsections we explain the rationale and construction of these models. Table 2 presents a summary of the different skull models that are generated.

Table 1: Conductivities for the reference head model.

	Tissue	Conductivity (S/m)	
■	Scalp	0.3333	[13]
■	Compact bone	0.0064	[1, 12]
■	Spongy bone	0.02865	[1, 12]
■	Air cavities	0.0000	[19]
■	Cerebrospinal Fluid	1.7857	[2]
■	White Matter	0.1428	[19]
■	Gray Matter	0.3333	[19]

2.1.1. Simplifications of the skull conductivity modeling: These models use the same geometry of the skull as the reference model but its conductivity modeling is simplified, generating models 1 to 3 as explained below (see Table 2). The air cavities in this case are modeled as in the reference model.

Model 1 – Isotropic heterogeneous skull (layCT). The skull is modeled as a heterogeneous compartment, but the spongy layer is not segmented from the CT image. It is constructed by iteratively eroding the compact layer six times with a 3×3 cross-shaped structuring element, until its thickness in the occipital region is below 5 mm [21]. Thus, it is an approximation to the actual layered structure of the skull. The conductivities for the compact and spongy bones are set as isotropic with the same values as those of the reference model.

Model 2 – Anisotropic homogeneous skull (aniCT). This model incorporates a single anisotropic skull compartment with air cavities, and uses its geometry to estimate the radial and tangential conductivities. For each voxel of the skull the normal and two orthogonal directions are derived, which in conjunction with the radial and tangential conductivities form the conductivity tensor. The anisotropy ratio of the skull used for this model is based on the works of [12, 8] which suggest ratios between 1:1.11 and 1:3.10 and on our own study on a spherical head model [24]. The radial conductivity is assumed to be 0.0105 S/m and the tangential 0.0191 S/m, i.e., an anisotropy ratio of 1:1.82 (radial:tangential) is used.

Model 3 – Isotropic homogeneous skull (isoCT). The skull is modeled as a homogeneous compartment with air cavities, having an isotropic conductivity of 0.0105 S/m. This value equals the radial conductivity of the anisotropic model because this conductivity has the strongest influence on the surface potential [34].

2.1.2. Simplifications of the skull geometry: Models 4 to 7 use a different geometry for the skull and air cavities, which are segmented from MR through the SPM8 toolbox. The conductivity values for all models are shown in Table 2 and correspond to the same as CT-based skull models explained in Section 2.1.1.

Model 4 – Isotropic heterogeneous skull (refMR). This model incorporates separate layers for the spongy and compact bones, all segmented from MR. A skull mask is extracted from MR using the SPM toolbox. This mask is overlaid with the original MR image and the resulting image is thresholded in order to distinguish between spongy and compact bones. The name given to this model is refMR because it corresponds to the most realistic skull segmented from MR.

Model 5 – Isotropic heterogeneous skull (layMR). The skull is modeled as a heterogeneous compartment, but the spongy layer is not segmented from the MR image as in model 4. It is constructed by iteratively erosion of the compact layer as explained for model 1.

Model 6 – Anisotropic homogeneous skull (aniMR). As explained for model 2, anisotropy is used to model the conductivity in this case.

Model 7 – Isotropic homogeneous skull (isoMR). The skull is modeled as a homogeneous isotropic compartment with air cavities, as described for model 3.









2.2. EEG source localization

The *forward problem* consists in finding the electrode potentials V at a specified scalp location, given a source inside the brain. Sources are modeled as single current dipoles, having position \mathbf{r} and orientation \mathbf{d} as their defining parameters. The surface potentials are related to the sources through the Poisson's equation:

$$\nabla \cdot (\Sigma \nabla V) = \nabla \cdot \mathbf{J}, \quad (1)$$

which is derived from the quasi-static approximation of the Maxwell equations, with Dirichlet and Neumann boundary conditions at each interface inside the head [32]. In (1), \mathbf{J} is the current density imposed by the dipole source and Σ is the conductivity tensor or matrix representing the direction-dependent conductivity. For isotropic conductivity, Σ is a diagonal matrix. However, for the anisotropic case Σ varies according to the position in the anisotropic compartment [14].

Table 2: Summary of the different skull models analyzed. For models 1 to 3, the skull was segmented from CT images while models 4 to 7 incorporate a skull segmented from MR. Models 1 and 5 use a spongy layer that corresponds to an erosion of the compact bone. Models 2 and 6 incorporate anisotropic conductivity (σ_{aniso}) while the other models use isotropic conductivities (σ_{iso}).

Simp.	Model	Tissue	Segmentation	Conductivity (S/m)	
-	Reference 	Compact	CT	$\sigma_{\text{iso}} = 0.0064$	
		Spongy	CT	$\sigma_{\text{iso}} = 0.02865$	
		Air cavities	CT	$\sigma_{\text{iso}} = 0.0$	
CONDUCTIVITY MODELING	1 layCT 	Compact	CT	$\sigma_{\text{iso}} = 0.0064$	
		Spongy	eroded compact	$\sigma_{\text{iso}} = 0.02865$	
		Air cavities	CT	$\sigma_{\text{iso}} = 0.0$	
	2 aniCT 	Compact + Spongy	CT	$\sigma_{\text{aniso}} \begin{cases} \sigma_{\text{rad}} = 0.0105 \\ \sigma_{\text{tang}} = 0.0191 \end{cases}$	
		Air cavities	CT	$\sigma_{\text{iso}} = 0.0$	
	3 isoCT 	Compact + Spongy	CT	$\sigma_{\text{iso}} = 0.0105$	
		Air cavities	CT	$\sigma_{\text{iso}} = 0.0$	
	GEOMETRY	4 refMR 	Compact	MR	$\sigma_{\text{iso}} = 0.0064$
			Spongy	MR	$\sigma_{\text{iso}} = 0.02865$
Air cavities			MR	$\sigma_{\text{iso}} = 0.0$	
5 layMR 		Compact	MR	$\sigma_{\text{iso}} = 0.0064$	
		Spongy	eroded compact	$\sigma_{\text{iso}} = 0.02865$	
		Air cavities	MR	$\sigma_{\text{iso}} = 0.0$	
6 aniMR 		Compact + Spongy	MR	$\sigma_{\text{aniso}} \begin{cases} \sigma_{\text{rad}} = 0.0105 \\ \sigma_{\text{tang}} = 0.0191 \end{cases}$	
		Air cavities	MR	$\sigma_{\text{iso}} = 0.0$	
7 isoMR 		Compact + Spongy	MR	$\sigma_{\text{iso}} = 0.0105$	
		Air cavities	MR	$\sigma_{\text{iso}} = 0.0$	

The relationship between the electrode potentials \mathbf{V}_{model} , the dipole location, $\mathbf{r} = (x, y, z)^T \in \mathbb{R}^{3 \times 1}$, and the dipole moments, $\mathbf{d} = (d_x, d_y, d_z)^T \in \mathbb{R}^{3 \times 1}$, can always be expressed as follows:

$$\mathbf{V}_{model}(\mathbf{r}, \mathbf{d}) = \mathbf{L}(\mathbf{r}) \cdot \mathbf{d}, \quad (2)$$

where $\mathbf{L}(\mathbf{r}) \in \mathbb{R}^{m \times 3}$ is the lead field matrix for a dipole at location \mathbf{r} .

The calculation of the forward problem is done with the *finite difference method* (FDM). For FDM the head is tessellated in a regular cubic grid resulting in a large number of nodes, and for each node a linear equation is obtained. To solve the large sparse linear system of equations resulting from the application of FDM, the *successive overrelaxation* (SOR) method is used. The SOR is an iterative solver that has to be reapplied for each source configuration and consequently the solution of the forward problem becomes too computationally expensive. Therefore, the *reciprocity theorem* is utilized to reduce the number of forward calculations performed with the iterative solver, making it equal to the number of electrodes. This speeds up the time necessary to do the forward calculations since the number of electrodes is much smaller than the number of dipoles [36, 16].

The FDM with reciprocity [36] that can incorporate anisotropies [17] (AFDRM) has been found to be suitable for solving the forward problem in realistic head models with anisotropic compartments, e.g. white matter [18] and skull [15], while the grid size is within 1 mm³. In addition, its accuracy as forward solver has been validated in combination with other methodologies [10, 5, 23, 6].

In this work, 128 electrode positions were used which were based on the 10/5 system [26], an extension of the International 10/20 system. The calculation grid of the AFDRM consisted of 5745427 nodes. The time required to compute the forward matrix using 128 electrodes was approximately 3 hours per electrode pair using one core of a CPU dual-socket quad-core Intel Xeon L5520 (Intel Nehalem microarchitecture, 2.27 GHz, 8 MB L3 cache per quad-core chip). Figure 2 presents a diagram explaining the steps necessary to generate the lead field matrix \mathbf{L} .

The *inverse problem* is defined as the estimation of the dipole parameters (\mathbf{r}, \mathbf{d}) that best fit a surface potential (\mathbf{V}_{in}). This is done by the minimization of the relative residual energy (RRE) [17]:

$$RRE = \frac{\|\mathbf{V}_{in} - \mathbf{V}_{model}(\mathbf{r}, \mathbf{d})\|_2^2}{\|\mathbf{V}_{in}\|_2^2} + \mathbf{C}(\mathbf{r}) \quad (3)$$

where \mathbf{V}_{in} is the set of given electrode potentials and $\mathbf{V}_{model}(\mathbf{r}, \mathbf{d})$ is the set of electrode potentials calculated by solving the forward problem in the models 1 to 7, respectively. The term $\mathbf{C}(\mathbf{r})$ is a penalization parameter which is zero when the dipole location is inside the grey matter and large otherwise. The minimization is done by the Nelder–Mead simplex method.

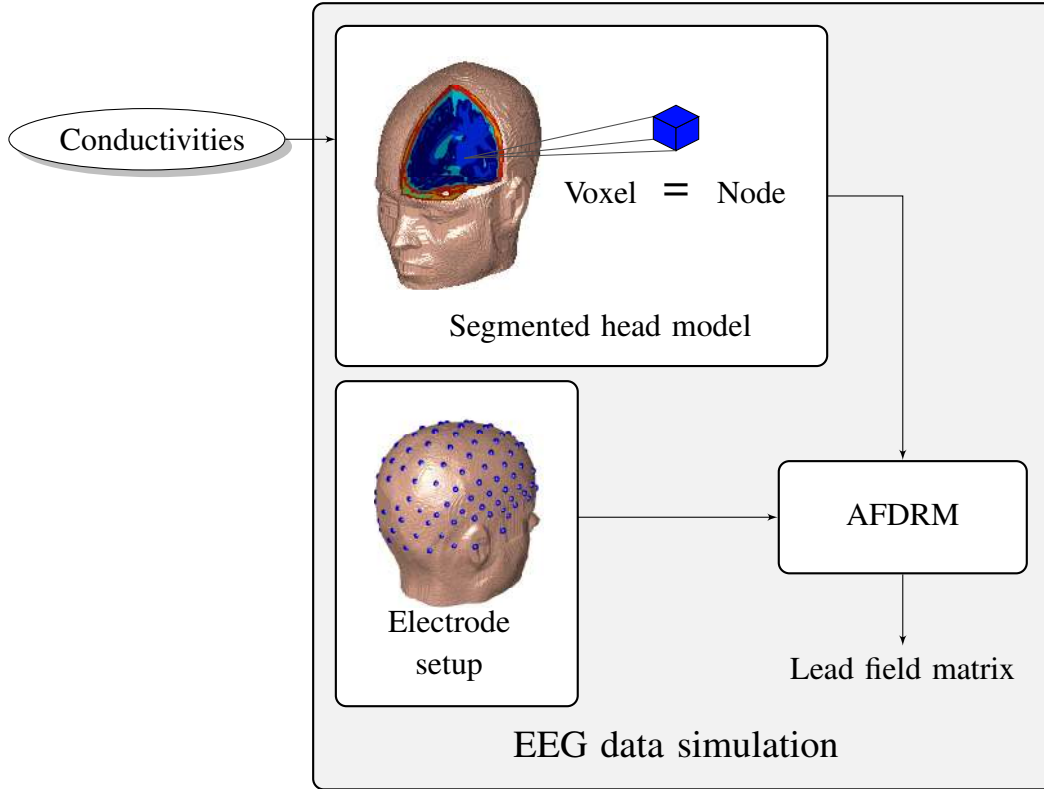


Figure 2: Diagram explaining the calculation of the lead field matrix. Conductivity values are assigned to the different tissues in the segmented head model. The voxels of this model correspond to the nodes of the AFDRM algorithm. For a given electrode setup and head model, the lead field matrix is calculated.

2.3. Simulation setup

We investigated the dipole localization and orientation errors due to using a simplified head model (model i , $\forall i \in 1, 2, 3, 4, 5, 6, 7$) instead of a more realistic one (reference model) in the dipole estimation. The diagram for the experimental setup can be seen in Figure 3.

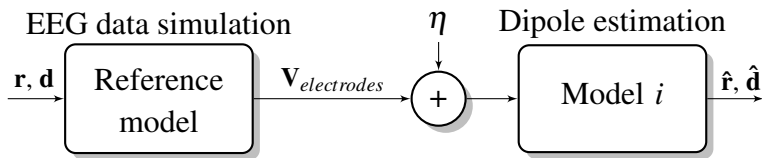


Figure 3: Simulation setup used to compare the reference model with the simplified head models (model i , $\forall i \in 1, 2, 3, 4, 5, 6, 7$). For each test dipole (\mathbf{r}, \mathbf{d}) , the electrode potentials $\mathbf{V}_{electrodes}$ were calculated by solving the forward problem in the reference model. From these potentials, the estimated dipoles $(\hat{\mathbf{r}}, \hat{\mathbf{d}})$ were obtained by solving the inverse problem in models 1 to 7. The sensitivity to noise of the different models was also analyzed by adding gaussian noise η with three different SNRs: 0, 5 and 10 dB.

Test dipoles were placed on a 3D grid with distance of 5 mm between each node. Only the nodes situated in the grey matter and above the lowest point in the electrode setup were considered, for a total of 8270 dipoles. Three orthogonal orientations were considered for each dipole location according to the Cartesian coordinate system: X-, Y- and Z-orientation.

Two different electrode setups were used so that the influence of spatial resolution could also be analyzed. From the initial setup of 128 electrodes, a subgroup of 32 were extracted following the standard 10/20.

For each test dipole with parameters \mathbf{r} and \mathbf{d} , the electrode potentials were calculated by solving the forward problem using the reference model. In this way, the simulated EEG data at the electrodes was obtained.

Subsequently, from the simulated potentials $\mathbf{V}_{electrodes}$, the dipoles were estimated by solving the inverse problem using models 1 to 7. Using the simulation setup displayed in Figure 3 we investigated the dipole location and orientation errors due to simplifications in the conductivity modeling of the skull (Models 1 to 3 vs. Reference). Furthermore, the influence of simplifying the geometry of the skull was also investigated (Models 4 to 7 vs. Reference).

Hence, the error due to the use of a simplified model in the solution of the inverse problem was investigated. The set of dipole parameters $\hat{\mathbf{r}}$ and $\hat{\mathbf{d}}$ which minimizes the cost function, are the estimated dipole parameters in the simplified head model.

The dipole localization error (DLE) was evaluated through the Euclidean distance between the original dipole location \mathbf{r} and the estimated dipole location $\hat{\mathbf{r}}$:

$$DLE = \|\hat{\mathbf{r}} - \mathbf{r}\|$$

The dipole orientation error (DOE), defined as the angle between the vector components of the original dipole \mathbf{d} and the estimated dipole $\hat{\mathbf{d}}$, was calculated through the cosine rule:

$$DOE = \arccos \frac{\hat{\mathbf{d}}^T \mathbf{d}}{\|\hat{\mathbf{d}}\| \|\mathbf{d}\|}$$

2.3.1. Sensitivity to noise: To analyze the sensitivity to noise of the different models, gaussian noise η was added to the simulated potentials $\mathbf{V}_{electrodes}$ with three different SNRs: 0, 5 and 10 dB. In order to perform a Monte-Carlo simulation, 100 trials were simulated for each dipole estimation and additive noise vector. The two electrode setups of 32 and 128 electrodes were compared again for the case with noise.

3. Results

3.1. Simplification of the skull conductivity modeling

To analyze the effects caused by the simplification of the skull conductivity modeling, we compared models 1, 2 and 3 against the reference model. These models have a CT-based geometry, i.e., the same geometry as the reference model but the conductivity is modeled as heterogeneous isotropic (layCT), homogeneous anisotropic (aniCT) and homogeneous isotropic (isoCT).

To understand the difference between the reference model and model 1 (layCT), Figure 4 displays the comparison of the spongy bone for both models. The spongy bone for model 1 is shown in red and the arrows indicate points where the largest amount of non-overlapping voxels are found. This information is taken into account for the analysis of the localization and orientation errors made by this model.

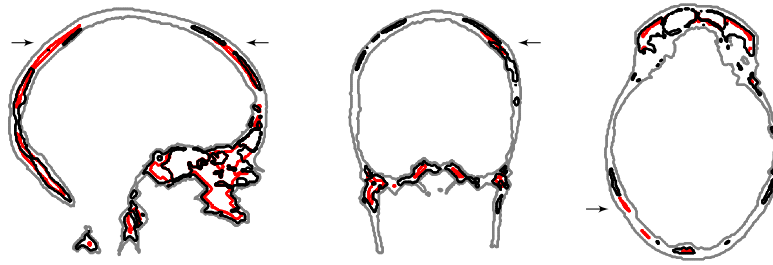


Figure 4: Superposition of spongy bones for skulls from Reference (in black) and Model 1 (in red). Arrows indicate the maximal difference between the spongy bone for both models.

Figure 5 shows the sagittal, coronal and axial views of both localization and orientation errors for models 1 to 3 with 128 electrodes. Among these three models, model 1 (Figure 5b) presents the overall lowest errors.

Localization errors for model 1, Figure 5b left side, are larger for deep sources in the brain than for superficial ones. By comparing homogeneous anisotropic and isotropic conductivity simplification as given by models 2 and 3, slightly lower errors are observed for the last model (Figure 5d). For these models, the localization errors are larger in the bottom (cerebellum) and in the superior parietal regions of the brain.

Orientation errors for model 1 are larger for superficial sources, with asymmetry towards the right side due to the differences in spongy bone between this and the reference model, as indicated by the arrow in the coronal view of Figure 4. The error pattern for models 2 and 3 exhibit great similarity but with rather larger errors for model 2, as concluded from the right side of Figures 5c and 5d.

The cumulative error histograms with 32 and 128 electrodes for models 1 to 3 are

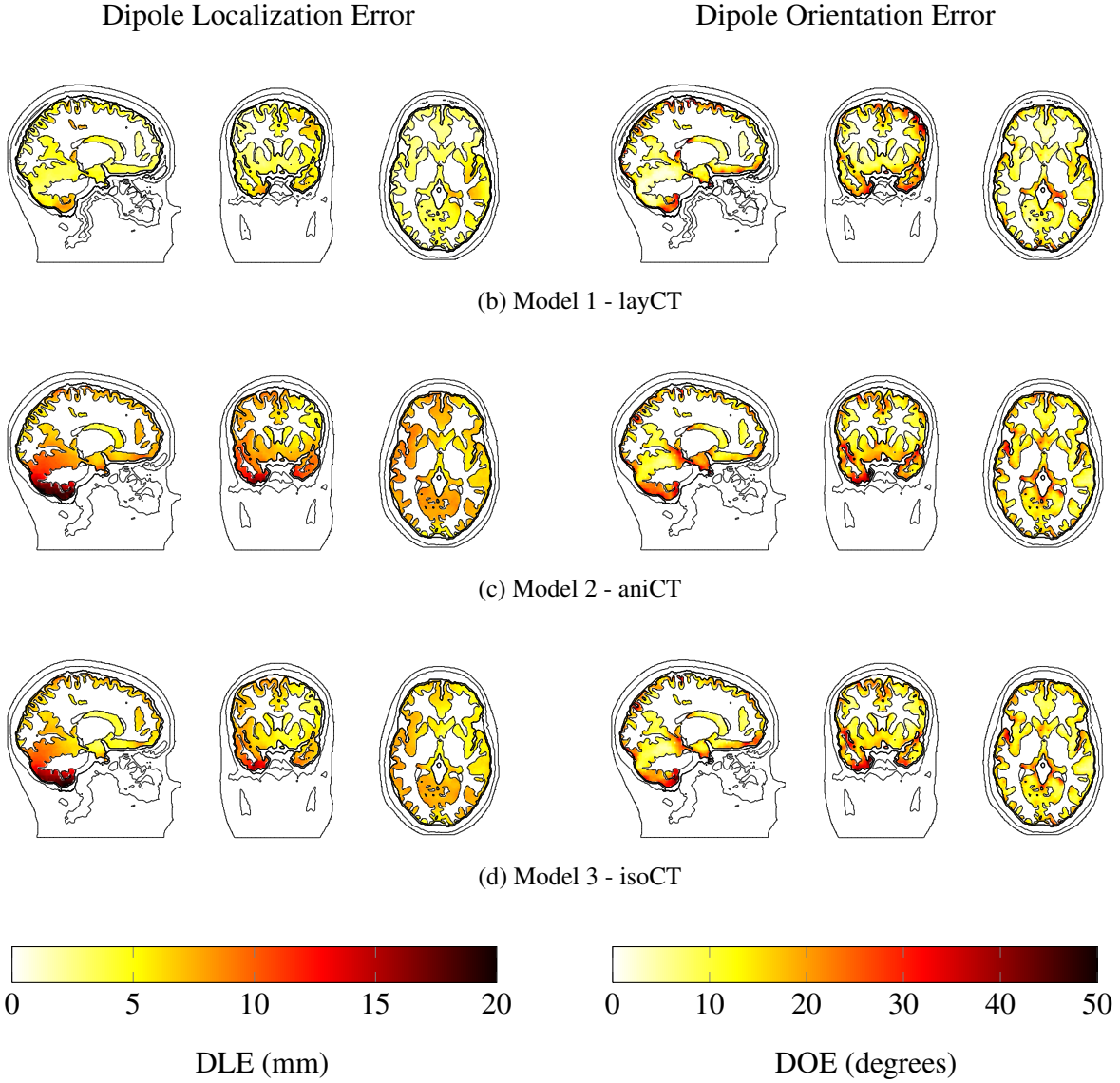
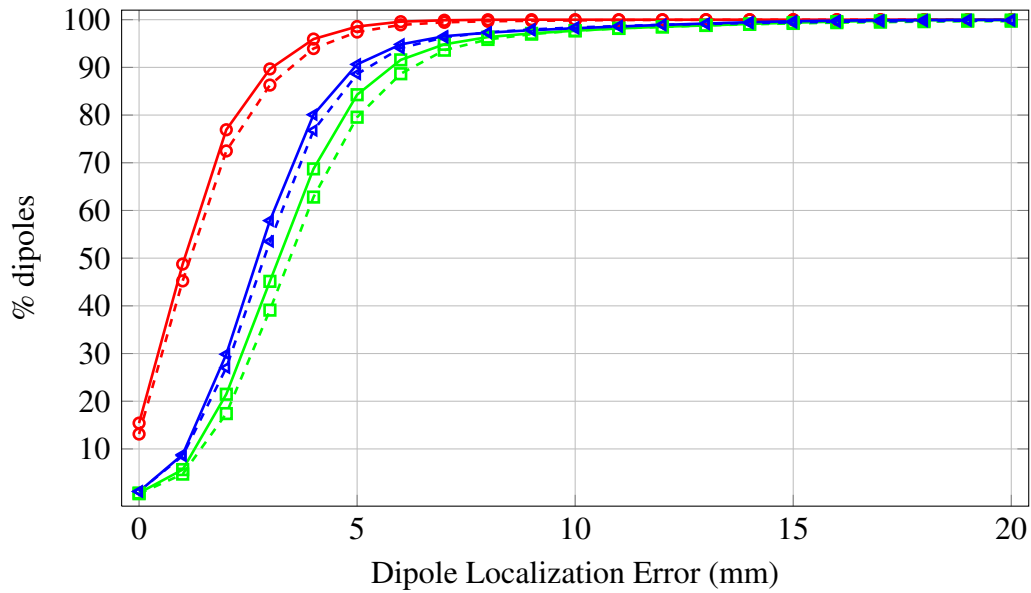


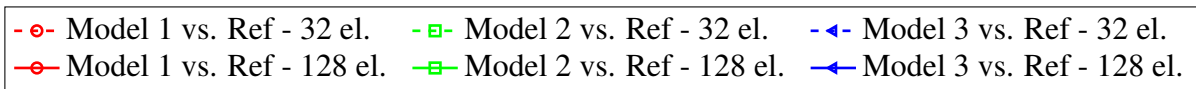
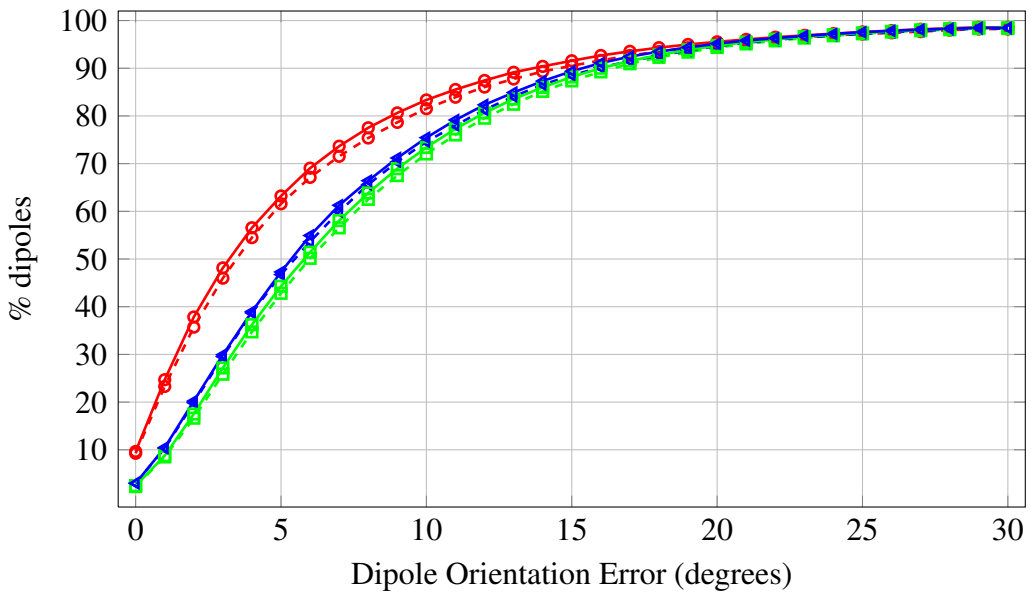
Figure 5: Dipole localization and orientation errors for the simplification of the skull conductivity modeling (CT-based skulls). The first column shows the dipole localization errors, while the second column displays the orientation errors for models 1 to 3 with 128 electrodes.

presented in Figure 6. The mean localization errors with 32 electrodes were 2.4 mm for model 1, 4.8 mm for model 2 and 4.2 mm for model 3. When 128 electrodes were used the errors decreased to 2.2 mm for model 1, 4.5 mm for model 2 and 4.0 mm for model 3. These results are presented in Table 3, for $\text{SNR} \rightarrow \infty$.

In the case of orientation errors, with 32 electrodes the mean orientation errors were 6.8° for model 1, 8.8° for model 2 and 8.4° for model 3. For the 128 electrodes configuration, the errors were 6.4° for model 1, 8.5° for model 2 and 8.2° for model 3.



(a) DLE - Models 1 to 3



(b) DOE - Models 1 to 3

Figure 6: Cumulative histograms of the dipole localization and orientation errors for the simplification of the skull conductivity modeling (CT-based skulls).

3.2. Simplification of the skull geometry

In this section, the influence of using simplifications of the skull geometry was analyzed through models 4 to 7. In this group, models 4 (refMR) and 5 (layMR) had a layered skull but with the spongy bone segmented in a different way. Models 6 (aniMR) and 7 (isoMR) incorporate a homogeneous skull either with anisotropic or isotropic conductivity.

To visualize more clearly the difference between the skulls segmented from CT and the ones segmented from MR, a visual comparison of their contours is shown in Figure 7. The contours of the CT-based skull is displayed in black and for the MR-based skull in red.

As can be seen in Figure 7a, the largest difference between the two models lie in the basal region of the skull, as the arrow indicates in the sagittal view. The segmentation of the air cavities has large correspondence for both modalities although for MR they are overestimated, as can be seen in Figure 7b.

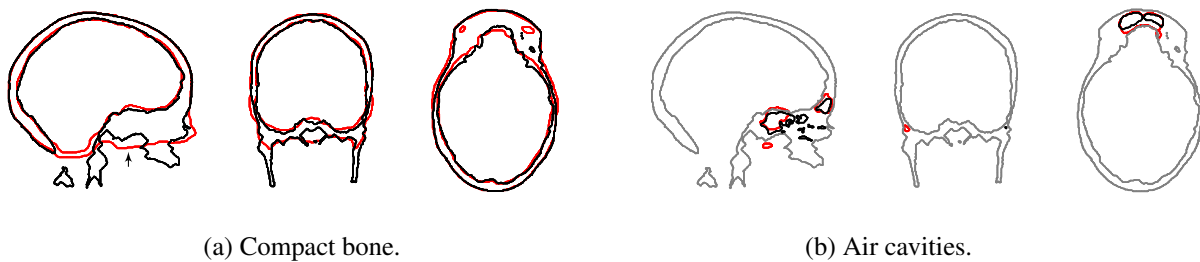
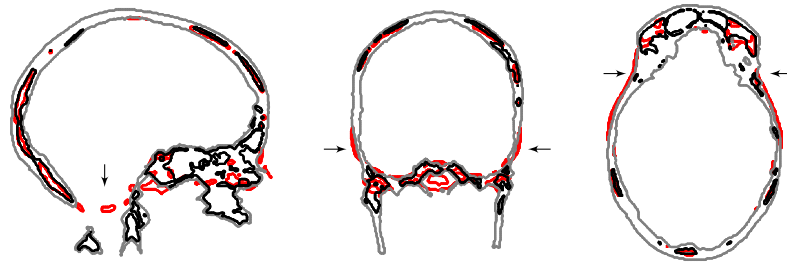


Figure 7: Superposition of contours for CT-based skull (in black) and MR-based skull (in red). Comparisons for the (a) compact bone and (b) air cavities are shown. Arrow in (a) indicates the maximal difference between the two contours.

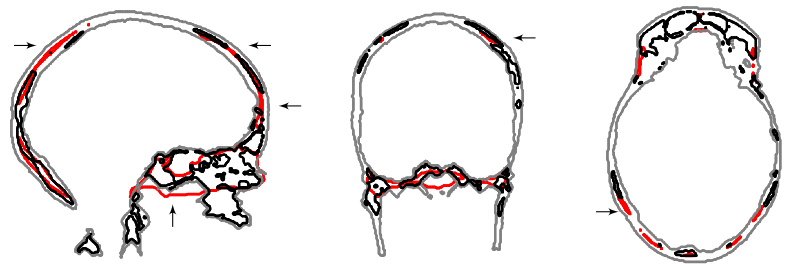
Figure 8 compares the spongy bones of the MR-based skulls versus the Reference model. When the spongy bone is compared for the skulls of Reference and Model 4, Figure 8a, errors in the skull thickness for the temporal and frontal regions are observed, which are segmented as spongy bone for the MR-based skull (see arrows). In spite of that, the spongy bone in the cranial vault corresponds largely for MR and CT based skulls. The most significant differences are found in the basal region of the skull.

The differences between the skulls of Reference and Model 5 can be seen mainly in the vault and base of the skull as pointed out by the arrows in Figure 8b.

Figure 9 shows the sagittal, coronal and axial views of both localization and orientation errors for models 4 to 7 with 128 electrodes. When the skull geometry is determined from MR images, the most visible errors are made in the basal region of the brain. This is concordant with the differences in the compact bone contours shown in Figure 7a.



(a) Reference vs. Model 4 – refMR.



(b) Reference vs. Model 5 – layMR.

Figure 8: Superposition of contours for Reference skull (in black) and spongy bone for skull (in red). Comparisons for the (a) compact bone, (b) spongy bone and (c) air cavities are shown. Arrow in (a) indicates the maximal difference between the two contours. In (b) arrows indicate parts of the MR-based skull model segmented incorrectly as spongy bone.

Localization errors for models 4 to 7 are large in the basal and bottom regions of the brain. For model 4, Figure 9b left, the errors for the superficial sources distributed along the cranial vault of the skull are small. In the case of model 5, Figure 9c, the errors made in the vault are slightly larger than for model 4 and are biased towards the right side of the brain. These findings are explained by the differences in spongy bone visualized in Figure 8. Models 6 and 7 exhibit a different localization error trend, the errors at the base are still large but less extended and in the vault the errors are in general larger than for models 4 and 5.

Orientation errors for models 4 to 7 are not only large at the base but also in the frontal region, close to where the air cavities lie. For models 4 and 5, Figure 9b and 9c right side, the errors seem to be more extended in the temporal and parietal lobes.

The cumulative histograms of the dipole localization and orientation errors are shown in Figure 10. As can be seen in this figure, the effect of using lower spatial sampling is more noticeable than for models 1 to 3. For the localization errors, Figure 10a, models 4 and 5 show a largest proportion (> 60%) of lower localization errors (< 5 mm) than models 6 and 7. Errors larger than 6 mm are present in greater proportion

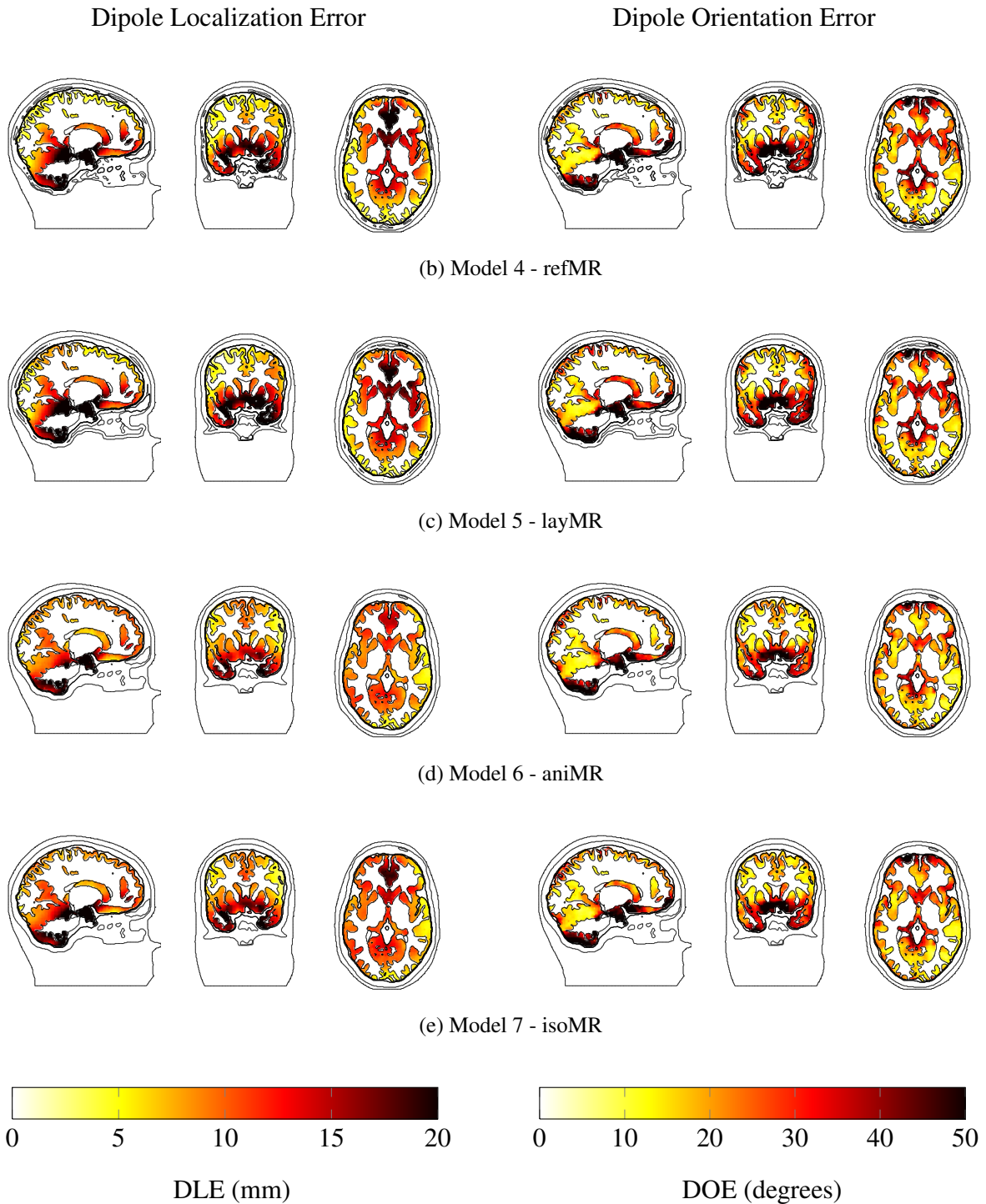
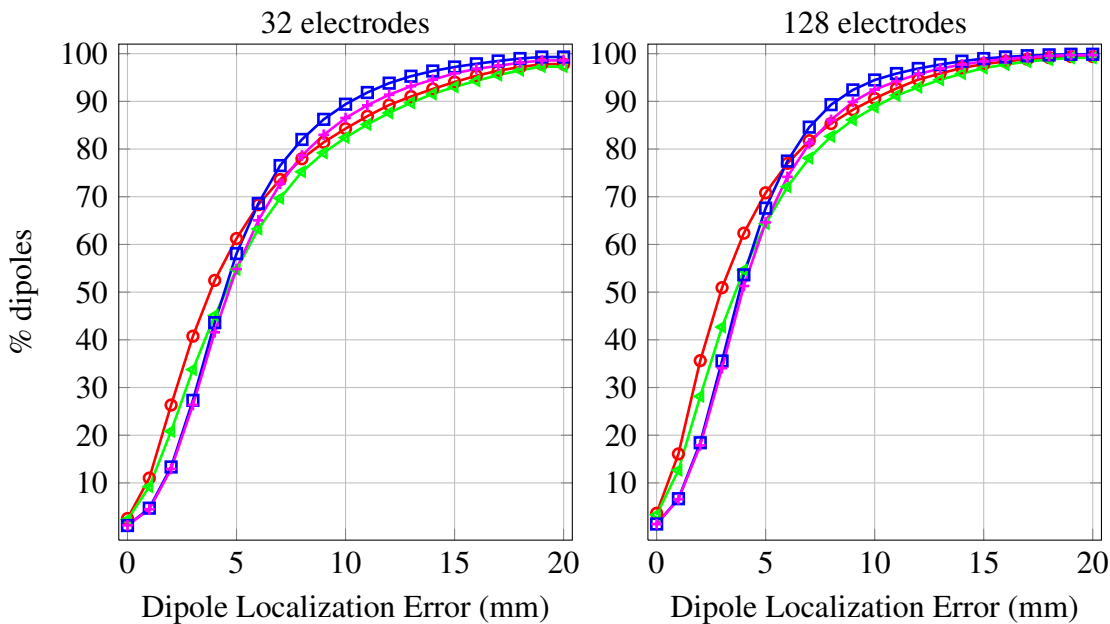
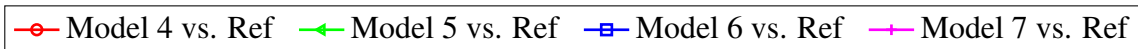
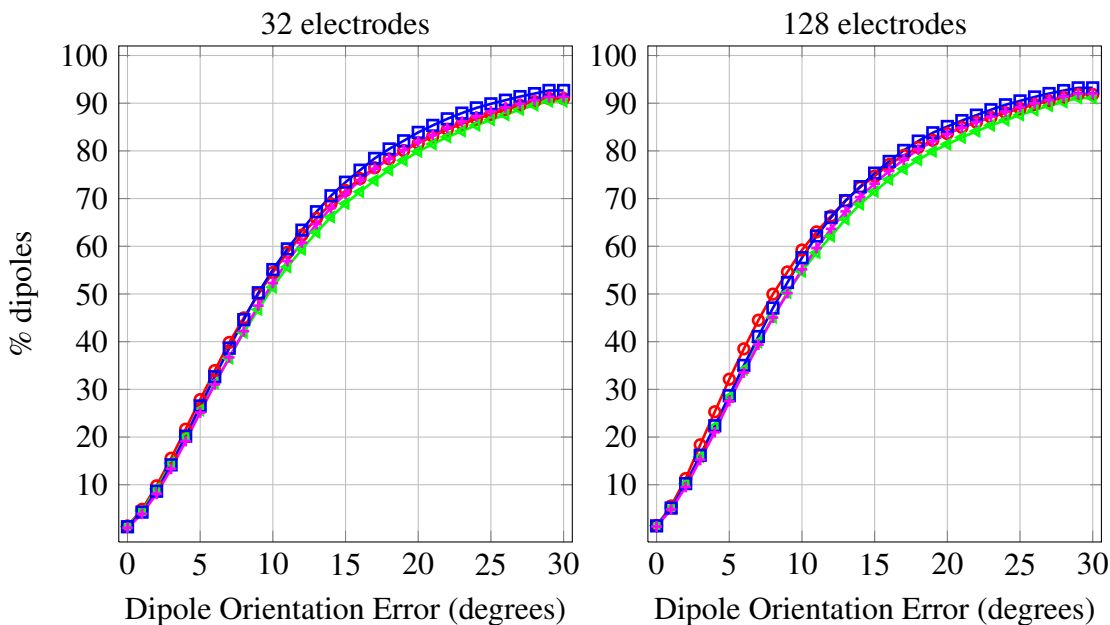


Figure 9: Dipole localization and orientation errors for the simplification of the skull geometry (MR-based skulls). The first column shows the dipole localization errors, while the second column displays the orientation errors for models 4 to 7 with 128 electrodes.



(a) DLE - Models 4 to 7 with 32 and 128 electrodes



(b) DOE - Models 4 to 7 with 32 and 128 electrodes

Figure 10: Cumulative histograms of the dipole (a) localization and (b) orientation errors for the simplification of the skull geometry (MR-based skulls).

in the homogeneous models (6 and 7), as shown in Figure 10a. For the orientation errors, Figure 10b, the cumulated errors for all the models are very close to each other, making the distinction more difficult. However, models 4 (refMR) and 6 (aniMR) can be considered in this group as the ones with the lowest orientation errors.

The mean localization errors for the 32 electrodes configuration were 6.3 mm for model 4, 6.9 mm for model 5, 6.3 mm for model 6 and 6.7 mm for model 7; with 128 electrodes the errors decreased to 5.1 mm for model 4, 5.7 mm for model 5, 5.4 mm for model 6 and 5.7 mm for model 7. These results are presented in Table 3, for $\text{SNR} \rightarrow \infty$.

For the orientation errors, with 32 electrodes the means were 13.5° for model 4, 14.1° for model 5, 13.0° for model 6 and 13.7° for model 7. For 128 electrodes, the means were 12.5° for model 4, 13.4° for model 5, 12.4° for model 6 and 13.0° for model 7.

3.3. Sensitivity to noise of the simplified models

The noise sensitivity of the different models was analyzed through a Monte-Carlo simulation as explained in Section 2.3.1. The mean dipole localization and orientation errors were obtained after addition of noise with three different SNRs: 0, 5, 10 dB and for the noiseless case ($\text{SNR} \rightarrow \infty$). Two different electrode setups were utilized in order to analyze the effect on the dipole estimation of using low (32 electrodes) and high (128 electrodes) spatial sampling in the presence of noise.

Table 3 and Figure 11 present the mean DLE for Reference and models 1 to 7 for noise and noiseless cases, with 32 and 128 electrodes. When $\text{SNR} = 0$ dB, the use of a particular model does not have any effect on the resultant DLE. However, a higher number of electrodes yields a lower DLE. At 5 dB, the choice of head model is not relevant if a 32 electrode setup is used. Using 128 electrodes, for CT-based models the lowest DLE is given by Model 1, while for the models based on MR the DLE does not differ greatly. Nevertheless, the smallest errors are made by models 4 and 6. At 10 dB, the influence of the electrode setup diminishes. When a CT is available, Model 1 yields the lowest DLE. Otherwise, when only MR is available, Model 4 is recommended. In the noiseless case, the difference between 32 or 128 electrode setup is very small. Nevertheless, the influence due to the increase in the number of electrodes is more notorious for the geometry than for the conductivity modeling simplification. Also in the noiseless case, Model 1 is the best model, when a CT is available.

The averages for the DOE are shown in Figure 12. In the case with the highest noise level, the differences for both electrode setups were $\sim 10^\circ$ for the CT-based models and $\sim 9^\circ$ for the MR-based models. With $\text{SNR} = 5$ dB, for the MR-based models the difference was $< 4^\circ$, while for the CT-based models it was $> 4^\circ$. For a SNR of 10 dB, the mean errors with 32 electrodes were larger for 1 to 2.5° than with 128 electrodes. In the

Table 3: Dipole localization errors for models 1 to 7 due to additive noise with SNRs 0, 5 and 15 dB. The SNR $\rightarrow \infty$ corresponds to the noiseless case. Each cell displays mean \pm standard deviation in mm.

	Model	SNR			
		0	5	10	∞
32 electrodes	Reference	33.2 \pm 17.9	11.9 \pm 5.7	4.2 \pm 2.1	0.0 \pm 0.1
	1 – layCT	33.4 \pm 17.9	12.2 \pm 5.7	4.8 \pm 2.2	2.4 \pm 1.5
	2 – aniCT	32.8 \pm 17.8	12.3 \pm 5.9	6.1 \pm 2.4	4.8 \pm 2.4
	3 – isoCT	32.8 \pm 17.8	12.2 \pm 5.8	5.7 \pm 2.4	4.2 \pm 2.2
	4 – refMR	33.2 \pm 17.7	13.0 \pm 6.0	7.4 \pm 2.6	6.3 \pm 4.9
	5 – layMR	33.5 \pm 17.8	13.3 \pm 6.0	7.9 \pm 2.5	6.9 \pm 5.0
	6 – aniMR	32.8 \pm 17.7	12.8 \pm 5.9	7.3 \pm 2.6	6.3 \pm 3.7
	7 – isoMR	32.9 \pm 17.7	13.0 \pm 6.0	7.6 \pm 2.6	6.7 \pm 4.2
128 electrodes	Reference	15.3 \pm 7.3	3.4 \pm 1.6	1.9 \pm 1.0	0.0 \pm 0.1
	1 – layCT	15.6 \pm 7.4	5.6 \pm 2.5	2.8 \pm 1.1	2.2 \pm 1.4
	2 – aniCT	15.4 \pm 7.4	6.6 \pm 2.7	4.8 \pm 1.1	4.5 \pm 2.3
	3 – isoCT	15.4 \pm 7.4	6.3 \pm 2.6	4.3 \pm 1.1	4.0 \pm 2.1
	4 – refMR	16.0 \pm 7.5	7.1 \pm 2.8	5.4 \pm 1.2	5.1 \pm 3.9
	5 – layMR	16.3 \pm 7.5	7.6 \pm 2.8	6.0 \pm 1.2	5.7 \pm 4.1
	6 – aniMR	15.6 \pm 7.5	7.1 \pm 2.8	5.6 \pm 1.2	5.4 \pm 3.0
	7 – isoMR	15.8 \pm 7.6	7.3 \pm 2.9	5.9 \pm 1.2	5.7 \pm 3.4

noiseless case, the difference was $< 1^\circ$. The trends displayed for the DOE are similar to those of the DLE (Figure 11).

4. Discussion

This study analyzed the dipole localization and orientation errors generated when a head model with simplified skull was used in the dipole estimation. In particular, a CT-based skull was used as reference. Two major simplifications were made: (i) in the conductivity modeling of the CT-based skulls and (ii) in the geometry through the use of MR-based skulls. In addition, the sensitivity to noise of the models was investigated through a Monte-Carlo simulation in which gaussian noise with three different SNRs was added. The use of high (128 electrodes) versus low (32 electrodes) spatial sampling was assessed in the noise study. The main goal was to determine guidelines for skull modeling in the generation of subject-specific head models in a clinical setup of epilepsy.

Our results suggest that the choice of a particular conductivity modeling for the skull depends on its geometrical accuracy. If the geometry is accurate, i.e., as derived from a CT image, the best option is to model the skull as layered isotropic. However, for a simplified geometry, as the one derived from an MRI, the conductivity can be modeled as

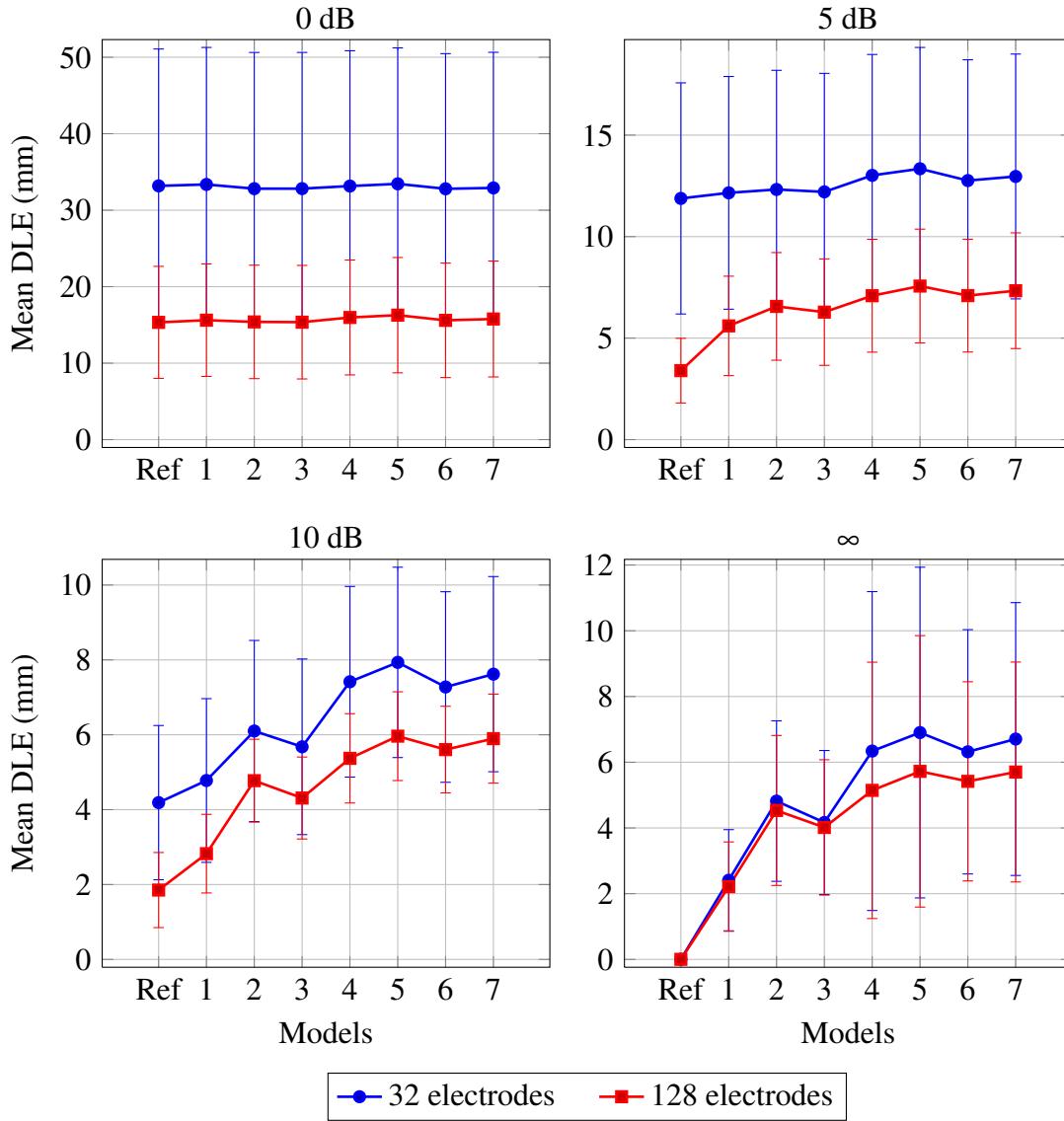


Figure 11: Mean localization errors for models 1 to 7 with 32 and 128 electrodes. Gaussian noise was added in each case with SNRs 0, 5 and 10 dB. The noiseless case corresponds to $\text{SNR} \rightarrow \infty$.

either layered isotropic or anisotropic. In the presence of noise in the EEG data, the use of a higher spatial sampling leads to smaller dipole estimation errors.

In the skull conductivity modeling simplification, the lowest errors were given by Model 1 (layCT) with isotropic heterogeneous skull. This result is in concordance with other studies [31, 8] in which it has been stated that modeling the layered isotropic compartment yields a better approximation of the skull than the anisotropic homogeneous modeling. Furthermore, in this work an erosion of the compact bone compartment resembled the actual spongiform layer of Model 1, which to our knowledge

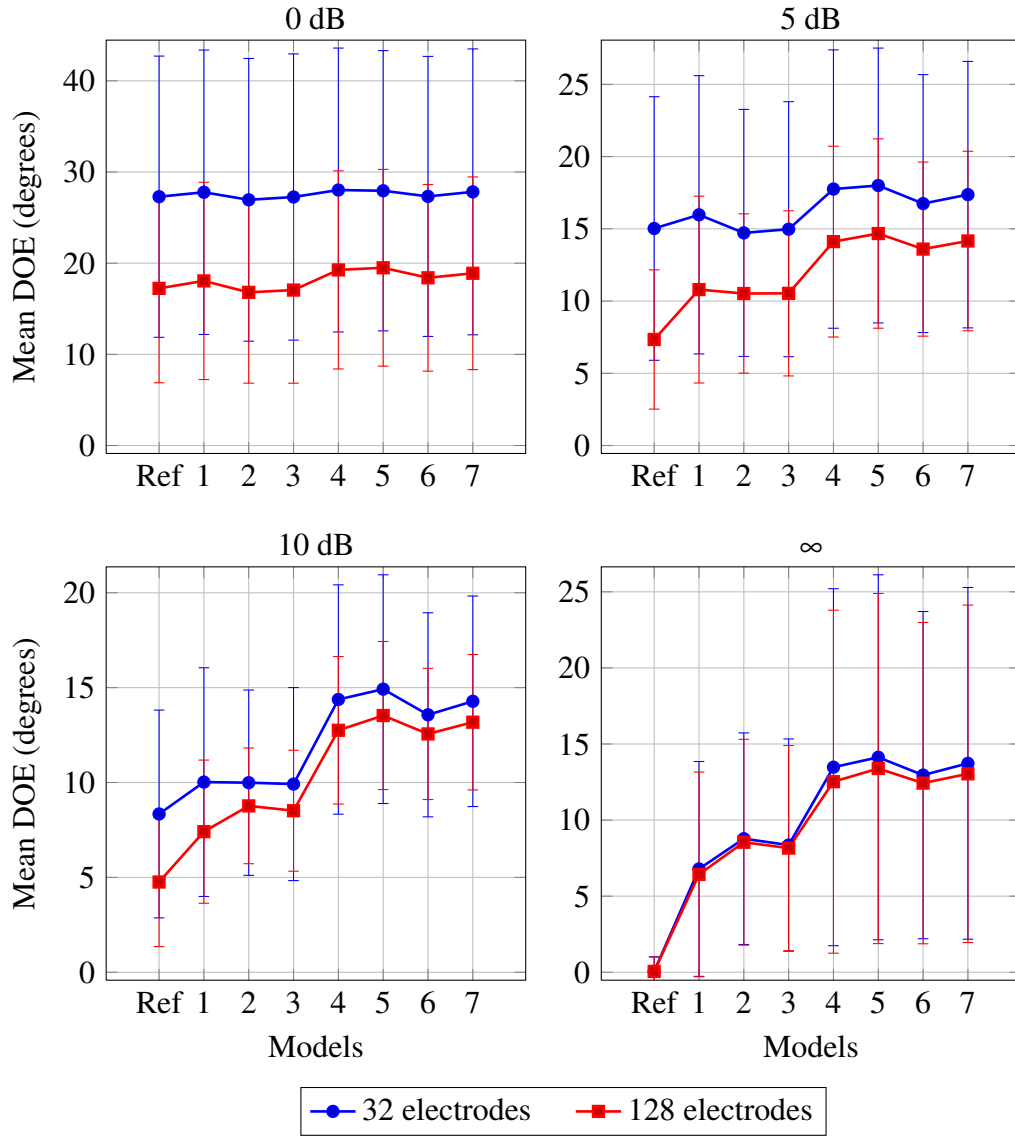


Figure 12: Mean orientation errors for models 1 to 7 with 32 and 128 electrodes. Gaussian noise was added in each case with SNRs 0, 5 and 10 dB. The noiseless case corresponds to $SNR \rightarrow \infty$.

has not been used before. Thus, when the skull geometry is segmented from CT, the conductivity modeling that yields the lower dipole estimation errors is given by isotropic heterogeneous.

In addition to the importance of modeling the layered structure of the skull, in this first simplification the results showed that modeling the conductivity as isotropic (Model 3 – isoCT) yielded lower errors than as anisotropic (Model 2 – aniCT). This can be explained on the first hand by the complicated geometry of the skull base. It has been shown [22, 37] that the determination of well-defined skull conductivity tensors requires

a smooth surface in order to obtain the radial skull anisotropy directions. In the case of Model 2, a smooth surface derived from the skull base might lead to tensors not accurately representing the geometry of this part of the skull. On the other hand, the conductivity value used for Model 3 was the same as the radial conductivity of Model 2 (0.0105 S/m), justified by the preponderance of radial over tangential conductivity [34]. These factors allowed isotropic homogeneous conductivity to obtain lower errors than anisotropy.

The second simplification performed on the skull was in the geometry by means of models 4 to 7 with MR-based skulls. In this group, models 4 and 5 had a layered skull but with the spongy bone segmented in a different way. For Model 4 (refMR) the spongy bone was obtained through thresholding of the MR image while for Model 5 (layMR) it was approximated as an erosion of the compact bone. Models 6 and 7 used a single compartment for the skull but the conductivity was approximated as either anisotropic or isotropic. For this simplification, large errors at the skull base were observed, mainly due to the wide differences in the basal region between the MR-based and Reference skulls (Figure 7). Although there was not a large difference in the localization errors between the models of this group, models 4 (refMR) and 6 (aniMR) presented the overall lowest errors. When the skull geometry is segmented from MR, isotropic heterogeneous or anisotropic conductivity modeling yield the lowest DLE.

For this simplification, contrary to the results for the conductivity modeling simplification, one of the models with isotropic heterogeneous skull (Model 5 – layMR) presented the largest average errors. However, the average error is not the only way to determine how good a model is. By examining the cumulative histograms of Figure 10a, it can be seen that with 128 electrodes Model 5 is better than models 6 and 7 for more than 50% of the dipoles. Nevertheless, the overall mean is lowered by large errors generated at the basal region due to overestimation of the skull spongiform layer in the base, and at the cortex due to its underestimation in the cranial vault.

According to the results discussed until here, anisotropy (Model 2 – aniCT) yielded the largest DLE for the conductivity modeling simplification but for the geometry simplification, Model 6 (aniMR) was among the best models. Although this might seem contradictory, what differs greatly between both models is the geometry of the skull base. While Model 2 has a very complex geometry, which explains why the anisotropic tensors were not so well defined for this area, Model 6 has much more simplified geometry at the skull base and therefore the tensors can better represent this geometry. Dannhauer et al. [8] found that the use of anisotropy to account for the layered surface of the skull did not yield a significant improvement. In our results, although using anisotropy yielded lower localization errors for the MR-based models, the difference between anisotropic (Model 6) and isotropic (Model 7) homogeneous models was not great according to Figure 10 and Table 3 for $\text{SNR} \rightarrow \infty$.

Huiskamp et al. [20] performed a simulation study in which the effect of using

head geometry based on MRI could be compared with the geometry based on CT. They generated four models with the inner and outer surfaces of the skull segmented in different ways. This study found that for a central source the use of actual geometry, as extracted from CT, will not improve much the localization errors. However, localization of mesial-temporal and basal frontal sources using realistic geometry based on MRI is far less accurate. This is in concordance with Figure 9, where the largest errors for MR-based models are seen in the basal part of the brain. Then, a CT is better representation of the skull and as a consequence a realistic geometry is better modeled using a CT. In contrast, air cavities and skull are difficult to distinguish in MRI.

The study of the noise sensitivity of the different models showed that the dipole estimation errors are high for high simulated noise levels (Figure 11). The accuracy of the models becomes more important for lower noise levels. In a very noisy environment, as the one depicted by SNR = 0 dB, the choice of a particular model is not relevant, however, the use of higher spatial sampling reduces considerably the DLE (~ 17 mm). For a real EEG signal with a typical SNR of 5 dB, there is an improvement in the DLE of ~ 6 mm when a higher number of electrodes is used. If an averaged spike is used for EEG source localization, which would correspond to a SNR of 10 dB, the importance of accuracy in the model becomes greater and the improvement in the DLE for the use of a higher spatial sampling is ~ 2 mm.

Limitations of the present study: (1) ref model is an approximation, (2) cond. values,

The accurate modeling of the skull is important in order to achieve results for EEG source localization that can be used in a clinical environment. However, the lack of precise conductivity values for the compact and spongy bones of the skull remain as a difficulty in the generation of a more accurate head model [27].

5. Conclusions

In order to use EEG source localization in a clinical environment, the following guidelines should be taken into account for the generation of patient-specific head models: (i) If there are CT images available, use them to model the geometry of the skull and its tissue types; (ii) when only MR images are available, the base of the skull should be modeled as accurately as possible; (iii) for an accurate geometry of the skull, the conductivity can be modeled as isotropic heterogeneous; (iv) for an approximate geometry of the skull, a hybrid model can be used for the conductivity modeling: at the base anisotropic and at the vault isotropic heterogeneous.

Future work: UTE

6. Acknowledgments

Victoria Montes Restrepo was funded by a grant of the Institute for BroadBand Technology (IBBT-iMIND). This work is funded by a research grant of the scientific research council of Flanders (FWO-Vlaanderen). The computational resources (Stevin Supercomputer Infrastructure) and services used in this work were provided by Ghent University, the Hercules Foundation and the Flemish Government – department EWI.

References

- [1] M. Akhtari et al. Conductivities of three-layer live human skull. *Brain Topography*, 14(3):151–167, 2002.
- [2] S.B. Baumann, D.R. Wozny, S.K. Kelly, and F.M. Meno. The electrical conductivity of human cerebrospinal fluid at body temperature. *IEEE Transactions on Biomedical Engineering*, 44(3):220–223, 1997.
- [3] V. Brodbeck, L. Spinelli, A.M. Lascano, M. Wissmeier, M.I. Vargas, S. Vulliemoz, C. Pollo, K. Schaller, C.M. Michel, and M. Seeck. Electroencephalographic source imaging: a prospective study of 152 operated epileptic patients. *Brain*, 134(10):2887–2897, 2011.
- [4] D.A. Brody, F.H. Terry, and R.E. Ideker. Eccentric dipole in a spherical medium: generalized expression for surface potentials. *IEEE Transactions on Biomedical Engineering*, BME-20(2):141–143, March 1973.
- [5] F. Chen, H. Hallez, and S. Staelens. Influence of skull conductivity perturbations on EEG dipole source analysis. *Medical Physics*, 37:4475, 2010.
- [6] G. Crevecoeur, V. Montes-Restrepo, and S. Staelens. Subspace electrode selection methodology for the reduction of the effect of uncertain conductivity values in the EEG dipole localization: A simulation study using a patient-specific head model. *Physics in Medicine and Biology*, 57:1963, 2012.
- [7] B.N. Cuffin. EEG localization accuracy improvements using realistically shaped head models. *IEEE Transactions on Biomedical Engineering*, 43(3):299–303, March 1996.
- [8] M. Dannhauer, B. Lanfer, C.H. Wolters, and T.R. Knösche. Modeling of the human skull in EEG source analysis. *Human Brain Mapping*, 32(9):1383–1399, 2011.
- [9] J.C. de Munck and M.J. Peters. A fast method to compute the potential in the multisphere model. *IEEE Transactions on Biomedical Engineering*, 40(11):1166–1174, November 1993.
- [10] I. Despotovic, W. Deburchgraeve, H. Hallez, E. Vansteenkiste, and W. Philips. Development of a realistic head model for EEG event-detection and source localization in newborn infants. In *Engineering in Medicine and Biology Society, 2009. EMBC 2009. Annual International Conference of the IEEE*, pages 2296–2299. IEEE, 2009.
- [11] K.J. Friston, editor. *Statistical parametric mapping: The Analysis of Functional Brain Images*. Academic Press Inc., U. S., 2006.
- [12] M. Fuchs, M. Wagner, and J. Kastner. Development of volume conductor and source models to localize epileptic foci. *Journal of Clinical Neurophysiology*, 24(2):101–119, 2007.
- [13] S.I. Gonçalves, J.C. de Munck, J.P.A. Verbunt, F. Bijma, R.M. Heethaar, and F. Lopes da Silva. In vivo measurement of the brain and skull resistivities using an eit-based method and realistic models for the head. *Biomedical Engineering, IEEE Transactions on*, 50(6):754–767, 2003.
- [14] H. Hallez. *Incorporation of anisotropic conductivities in EEG source analysis*. PhD thesis, Ghent University, 2008.

- [15] H. Hallez, S. Staelens, and I. Lemahieu. Dipole estimation errors due to not incorporating anisotropic conductivities in realistic head models for EEG source analysis. *Physics in Medicine and Biology*, 54:6079–6093, 2009.
- [16] H. Hallez, B. Vanrumste, R. Grech, J. Muscat, W. De Clercq, A. Vergult, Y. D’Asseler, K.P. Camilleri, S.G. Fabri, S. Van Huffel, et al. Review on solving the forward problem in EEG source analysis. *Journal of NeuroEngineering and Rehabilitation*, 4(1):46, 2007.
- [17] H. Hallez, B. Vanrumste, P.V. Hese, Y. D’Asseler, I. Lemahieu, and R.V. Walle. A finite difference method with reciprocity used to incorporate anisotropy in electroencephalogram dipole source localization. *Physics in Medicine and Biology*, 50:3787–3806, 2005.
- [18] H. Hallez, B. Vanrumste, P.V. Hese, S. Delputte, and I. Lemahieu. Dipole estimation errors due to differences in modeling anisotropic conductivities in realistic head models for EEG source analysis. *Physics in Medicine and Biology*, 53:1877–1894, 2008.
- [19] J. Haueisen, C. Ramon, P. Czapski, and M. Eiselt. On the influence of volume currents and extended sources on neuromagnetic fields: A simulation study. *Annals of Biomedical Engineering*, 23(6):728–739, 1995.
- [20] G. Huiskamp, M. Vroeijsstijn, R. van Dijk, G. Wieneke, and A.C. van Huffelen. The need for correct realistic geometry in the inverse EEG problem. *IEEE Transactions on Biomedical Engineering*, 46(11):1281–1287, November 1999.
- [21] N. Lynnerup, J.G. Astrup, B. Sejrsen, et al. Thickness of the human cranial diploe in relation to age, sex and general body build. *Head & Face Medicine*, 1(13), 2005.
- [22] G. Marin, C. Guerin, S. Baillet, L. Garnero, and G. Meunier. Influence of skull anisotropy for the forward and inverse problem in EEG: simulation studies using FEM on realistic head models. *Human Brain Mapping*, 6(4):250–269, 1998.
- [23] V. Montes-Restrepo, H. Hallez, and S. Staelens. Influence of skull inhomogeneities on EEG source localization. In *Noninvasive Functional Source Imaging of the Brain and Heart & 2011 8th International Conference on Bioelectromagnetism (NFSI & ICBEM), 2011 8th International Symposium on*, pages 72–76, may 2011.
- [24] V. Montes-Restrepo and S. Staelens. Determination of anisotropic ratio of the skull for EEG source localization in patients with epilepsy. In *Abstracts of the 11th FirW PhD Symposium*, page 62, Ghent, Belgium, 2010. Ghent University.
- [25] P.L. Nunez and R. Srinivasan. *Electric Fields of the Brain: The Neurophysics of EEG*. Oxford University Press, New York, 2005.
- [26] R. Oostenveld and P. Praamstra. The five percent electrode system for high-resolution EEG and ERP measurements. *Clinical Neurophysiology*, 112(4):713–719, 2001.
- [27] R. Pohlmeier, H. Buchner, G. Knoll, A. RienÄcker, R. Beckmann, and J. Pesch. The influence of skull-conductivity misspecification on inverse source localization in realistically shaped finite element head models. *Brain Topography*, 9:157–162, 1997. 10.1007/BF01190384.
- [28] C. Ramon, P.H. Schimpf, and J. Haueisen. Influence of head models on EEG simulations and inverse source localizations. *Biomedical Engineering Online*, 5, 2006.
- [29] M. Rullmann, A. Anwander, M. Dannhauer, S.K. Warfield, F.H. Duffy, and C.H. Wolters. EEG source analysis of epileptiform activity using a 1 mm anisotropic hexahedra finite element head model. *NeuroImage*, 44(2):399–410, 2009.
- [30] S. Rush and D.A. Driscoll. Current distribution in the brain from surface electrodes. *Anesthesia and analgesia*, 47(6):717–723, 1968.
- [31] R.J. Sadleir and A. Argibay. Modeling skull electrical properties. *Annals of Biomedical engineering*, 35(10):1699–1712, 2007.
- [32] J. Sarvas. Basic mathematical and electromagnetic concepts of the biomagnetic inverse problem.

- Physics in Medicine and Biology*, 32:11–22, 1987.
- [33] M. Stenroos and J. Sarvas. Bioelectromagnetic forward problem: isolated source approach revis(it)ed. *Physics in Medicine and Biology*, 57(11):3517, 2012.
 - [34] S. Vallaghé and M. Clerc. Conductivity Estimation for EEG: What is Relevant? In *Noninvasive Functional Source Imaging of the Brain and Heart and the International Conference on Functional Biomedical Imaging, 2007. NFSI-ICFBI 2007. Joint Meeting of the 6th International Symposium on*, pages 369–372. IEEE, 2007.
 - [35] B. Vanrumste, G. Van Hoey, R. Van de Walle, M. D’Havé, I. Lemahieu, and P. Boon. Dipole location errors in electroencephalogram source analysis due to volume conductor model errors. *Medical and Biological Engineering and Computing*, 38(5):528–534, 2000.
 - [36] B. Vanrumste, G. Van Hoey, R. Van de Walle, M. D’Havé, I. Lemahieu, and P. Boon. The validation of the finite difference method and reciprocity for solving the inverse problem in EEG dipole source analysis. *Brain Topography*, 14(2):83–92, 2001.
 - [37] C.H. Wolters, A. Anwander, X. Tricoche, D. Weinstein, M.A. Koch, and R.S. MacLeod. Influence of tissue conductivity anisotropy on EEG/MEG field and return current computation in a realistic head model: A simulation and visualization study using high-resolution finite element modeling. *NeuroImage*, 30(3):813–826, 2006.